Master's Thesis Project

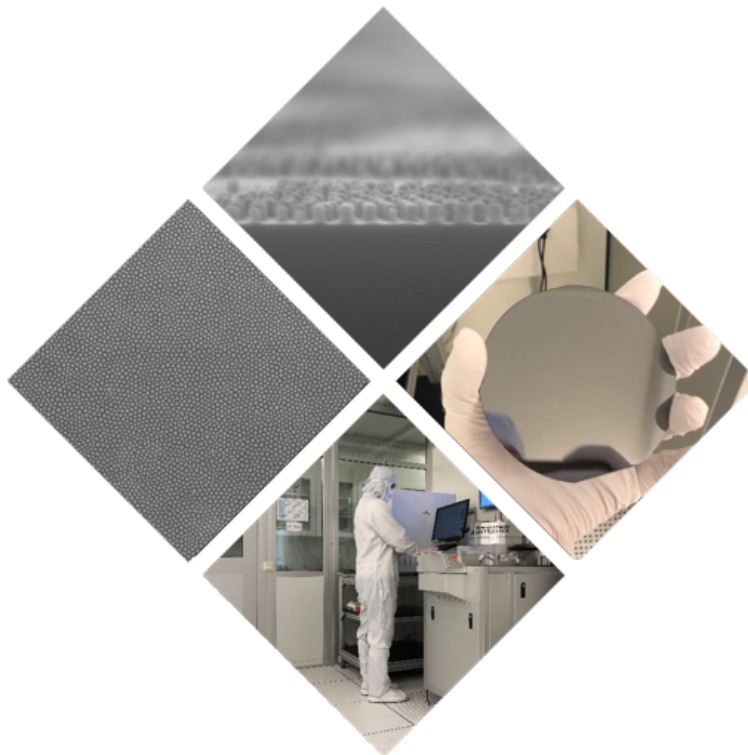## Lunds Tekniska Högskola
Engineering Nanoscience

Block copolymer-based hybrid nanomaterials for nanoimprint applications

---

Author:
Philip Sellin

Supervisor:
Ivan Maximov

February 21, 2022

Abstract

In this Master's thesis project, a block copolymer (BCP) film was used in combination with sequential infiltration synthesis and etching to manufacture a nanoimprint lithography stamp consisting of silicon. The BCP film was designed to contain perpendicularly aligned hexagonally placed cylinders, a pattern that will later be investigated for antibacterial properties after being transferred via nanoimprint lithography to a polymer film. To facilitate satisfactory pattern transfer from the BCP film into the silicon, optimisation of the infiltration conditions were made. During this process, thermal annealing was observed to induce self-assembly of the BCP PS-b-P4VP into perpendicularly aligned cylinders that were locally hexagonally placed. The nanoimprint lithography stamp was found to achieve the transfer of the cylindrical pattern into a polymer film that will later be evaluated for its antibacterial properties.

1

Contents

Acknowledgements

There are a lot of people I have to thank for their crucial help during this project. Firstly, Ivan Maximov, who was the one to actually come up with the idea for this Master's thesis project, thank you. Apart from that, I also want to express my thanks for all the valuable feedback I have gotten throughout the project from you.

During this Master's thesis project I have encountered unfamiliar subjects and have felt lost at times. For example when not understanding how to use a tool in the cleanroom and when introduced to the intricacies of self-assembly. If it were not for Anette Löfstrand, I would have probably mistakenly broken half of the tools available in the cleanroom by now. I would also like to thank you Anette for the patience you have shown when I repeatedly asked similar questions because I had troubles grasping that subject.

I also want to express my thanks to Nicklas Nilsson and Vladislav Genevskiy, with whom collaboration have taken place, for their input about the results of the samples processed. Furthermore, thank you Nicklas for the feedback on the nanoimprint lithography parts of my report as well as your infectious enthusiasm expressed throughout this project.

There are lots of people that have helped teach me how to operate the equipment in the cleanroom, among these are Reza Jafari Jam, Peter Blomqvist and Dmitry Suyatin. Thank you all, who helped me in this regard, for your guidance.

To my family, thank you for all the emotional support you have provided when I have felt down and stressed. Moreover, thank you for listening when I have talked endlessly about the amazingly cool equipment I have been able to use during this project.

To my cousin Elias Grape, with whom I can always discuss technical subjects and who was also my roommate during part of this project, thank you for all the support; from mental support to information about how you approached your Master's thesis project.

Apart from this, I also would want to extend my thanks to every other person who have helped me on this journey that I have not thanked explicitly.

Finally, last, but certainly not least, thank you Camilla for being my rock during this project. Thank you for all the support whenever I have needed it and for being a refuge in all the stress.

1 Introduction

In the field of nanoprocessing, optical lithography has been widely utilised to manufacture nanostructures. In recent years though, block copolymers (BCP) have gained interest for nanostructure fabrication. These speciality polymers can self-assemble at the nanoscale forming certain structures, among others, hexagonally placed cylinders and lamellar shapes [1]. In this Master's thesis, BCP films containing locally hexagonally placed cylinders were utilised as etch masks in a reactive ion etching (RIE) process. The aim was to manufacture silicon wafers onto which the pattern from a BCP film was transferred via etching, i.e. the cylinders should consist of silicon after all processing steps. These silicon wafers were manufactured to be used as nanoimprint lithography (NIL) stamps. Using these stamps, in collaboration with Malmö University and the company Obducat, the pattern was transferred via nanoimprint lithography to plastic films that were then examined to find out whether the pattern had antibacterial properties or not. Although this was not part of the Master thesis project since it was carried out by the collaborators, it served as motivation for the whole thesis project. It was therefore of great importance to understand both the nanoimprint lithography process, as well as the effect patterns can have on antibacterial properties. Furthermore, it is important to understand what alternative manufacturing techniques exist and the benefits and drawbacks they come with.

2 Background

To achieve the cylindrical structure of silicon mentioned in the introduction, various techniques were utilised. These techniques are explained in the following sections. To understand how the nanopattern was created, the section about block copolymers is key, additionally, the sections about sequential infiltration synthesis and reactive ion etching are of great importance to understand the processing steps. Furthermore, the section on NIL and antibacterial properties serves as great background information to understand the constraints and properties of the finished silicon wafer.

2.1 Block Copolymers

A block copolymer (BCP) consist of different polymer chains covalently linked to each other, where one chain is usually polar and the other non-polar [1]. The way they are linked can be varied extensively, but one widely used arrangement is the coil-coil diblock copolymer [1]. The coil-coil distinction means the BCP does not contain any rigid-rod block [1]. These BCPs are typically forming self-assembled structures where one of the polymer chains, i.e. on of the blocks, forms a shape, for example spheres or cylinders, while the other polymer chain in the same BCP forms a matrix around the shape. Examples of BCPs are polystyrene-block-poly(methyl methacrylate) (PS-b-PMMA), which a great deal of the block copolymer research has been focused on, and polystyrene-block-poly(4-vinylpyridine) (PS-b-P4VP), which will be used in this thesis project. In the case of PS-b-P4VP, polystyrene (PS) and poly(4-vinylpyridine) (P4VP) chains are joined together covalently. The structure of this block copolymer can be seen in Figure 1.
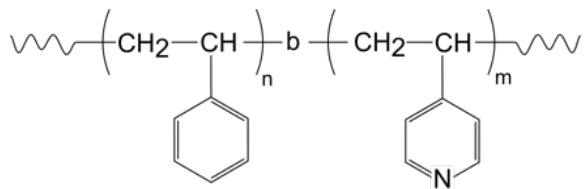
Figure 1: Schematic image of the molecular structure of PS-b-P4VP where the PS and P4VP parts are joined together covalently [2]. Notice that the curved chain to the left and right indicates the presence of end groups.

2.1.1 Self-assembly of Block Copolymers

Block copolymers can self-assemble because of thermodynamical incompatibility of the polymer chains that are covalently joined in a block copolymer [1]. This incompatibility gives rise to phase separation in the nanometer range [3]. The term microphase separation accurately describes the self-assembly process [3]. This means that the BCP system maximises attractive interactions between the polymer blocks while minimising the repulsive interactions [3]. Hence, the BCP segregates into domains of the individual blocks [3]. Furthermore, since the polymer blocks are joined together with a

covalent bond, the scale at which the microphase separation occurs is comparable to the size of the block copolymer chains [3]. Therefore, by changing the molecular weight of the copolymer, the size and separation distances of the self-assembled structure can be tuned and depending on the compositions of the blocks in the BCP, different shapes can be achieved during self-assembly [4].

For diblock copolymers, sphere, cylindrical, gyroid and lamellar shapes are attainable [1], this can be seen in Figure 2.

The microphase separation of block copolymers is a true self-assembly process which means that at a critical temperature, denoted the order-to-disorder transition temperature T_{ODT}, the entropy effect of the polymer chain movements will dominate the enthalpic effects of the intermolecular forces [1, 3]. This implies that the ordered arrangement of a BCP is limited to a certain temperature range [3]. Moreover, above a specific temperature for each polymer, called the glass transition temperature, mobility is increased due to decreased viscosity and increased diffusion of said polymer, meaning rearrangements are more easily achieved [5]. Since a BCP most likely will be subjected to room temperature at some point in its lifetime, at least one of the polymer blocks in the BCP should have its glassy state above room temperature to inhibit rearrangements [3]. The polymers in the blocks used in this thesis project have a glass transition temperature, T_g, of 102°C and 147°C respectively. Furthermore, the order-to-disorder temperature of the BCP used is well beyond 300°C [6].

There have been many theories trying to predict the order-to-disorder transition temperature T_{ODT} for various block copolymers, one such theory is the self-consistent mean-field theory (SCFT) [7]. Using this theory, the following diblock copolymer phase diagram, see Figure 2, has been produced [7]. Notice that with increasing volume fraction of one block, f, the system passes through the structures mentioned above as long as the system is over T_{ODT}. From left to right, with increasing f, the system passes through closely packed spheres (CPS) onto body-centred cubic spheres (Q^{229}), hexagonally packed cylinders (H) through the bicontinuous gyroid shape (Q^{230}) and finally to the lamellar shape (L)[1]. The same structures appear in reverse as f is increased over 0.5, but then the specific polymer in the majority and the minority blocks are swapped in the microdomains, for example from the matrix to the hexagonally packed cylinders. In the phase diagram, it is also possible to find the predicted order-to-disorder transition temperature T_{ODT} by looking at the line that separates the structures mentioned above with

the last field, which denotes the disordered state found at the bottom and to the left and right of the phase diagram. Apart from the microdomain structures mentioned above, if the block copolymer is manufactured to be joined in another way, for example, a ring, star or by using triblock copolymers, additional shapes can be obtained [1, 8].
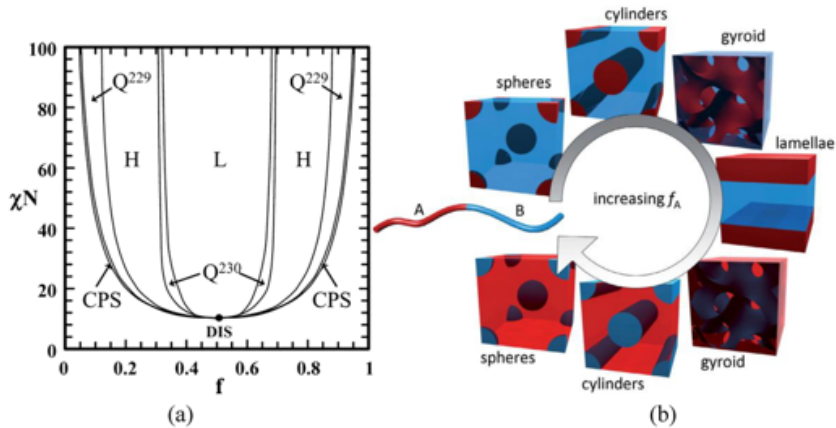

Figure 2: In a), phase diagram for coil-coil diblock copolymers is presented. In b), it is seen that changing the composition of block A and B results in the different structures mentioned before [9].

Using the phase diagram above, it is straightforward to choose reasonable volume fractions of the individual polymer parts to obtain the desired structure. However, even if hexagonally arranged cylinders are formed in the sample, the orientation they align can be undesired if care is not taken [3]. This alignment of the resulting self-assembled structure can be affected by the interface between the air and the BCP, as well as the substrate to BCP interface [3]. Both the lamellar structure and the hexagonal cylindrical structure can align parallel to the substrate surface instead of perpendicular to said direction [3]. This typically happens when one of the blocks selectively wets an interface, leading to segregation of that polymer block there [3]. To combat this, it is often needed to control the surface hydrophobicity, which affects the surface and adlayer interactions, to obtain the orientation and alignment of the BCP structures [10]. One approach often utilised is to control the substrate to BCP interface with a polymer brush layer [3]. This layer can be made of a copolymer whose composition is controlled, to obtain the wanted surface energy and chemistry [3]. It is worth noting that

7

there exist other ways to solve this problem, one such way being to use a self-assembled monolayer [3]. Albeit, adding an additional layer under the BCP film might pose problems if the BCP film is later used as an etch mask, meaning it is preferable if there is no need for any brush layer at all.

When a BCP is spin-coated, it does not typically contain the self-assembled pattern sought but rather defect-rich morphologies that are kinetically trapped [11]. The reason for this is at least partially due to rapid evaporation of the solvents used for spinning which leaves the spin-coated BCP in a thermal non-equilibrium [11]. To get the BCP to self-assemble into the desired structure, a method to induce self-assembly in the BCP is typically used [4]. With self-assembly, small regular structures suitable for lithography can be formed, with a size dimension of less than 100 nm [12]. Among the methods to induce this self-assembly are for example electric fields, shear forces, thermal annealing and Solvent Vapour Annealing (SVA) [13, 14]. Although these techniques can achieve great ordering, it is worth mentioning that it is a considerable challenge to produce nanoscopic patterns that are maintained perfectly on macroscopic length scales [15].

2.1.2 Solvent Vapour Annealing

In solvent vapour annealing (SVA), evaporation of solvents is used to form a highly directional solvent concentration field that directs the self-assembly of the BCP film, with ordering initiated at the surface of the BCP film then propagating downwards into the film [4]. The way solvent vapour annealing causes the BCP to restructure is through increased mobility of the polymer chains during solvent swelling of the BCP film due to a decrease of the T_g, which is caused by the solvents used [13]. When the mobility is increased, the BCP system can start to restructure in an energetically favourable way [13].

There is a multitude of parameters affecting the results of SVA. Among these are the composition of the polymer blocks, f_A and f_B, the degree of polymerisation N, the Flory-Huggins interaction parameter χ_{AB} which describes the segment-segment interactions between the two polymer blocks, the thickness h of the BCP film and the surface tensions of the two microdomains, γ_A and γ_B [11]. Additionally, the chemical and topological properties of the substrate can allow for interactions between the substrate and any of the polymer blocks which too can affect the result of the SVA [11]. Moreover, the solvents that are used to induce the self-assembly affects the

result of SVA. It is mainly the quality and selectivity of the solvents to the two blocks that are of importance. These solvents affect the kinetics and the pathways of the structural changes in the BCP film, hence it can also affect the final structure of the BCP film [11]. Under some SVA conditions, a non-equilibrium structure is created, believed to be caused by large solvent flows through the polymer during drying [11]. However, these non-equilibrium structures that can be created with SVA are not well understood yet [11]. In general, when performing SVA, a BCP film is usually taken from a thermal non-equilibrium to a thermal equilibrium [11].

For BCP films that are prepared on solid substrates with a free polymer to air interface, islands or holes are often present in the film resulting in an uneven thickness of said BCP film [11]. The reason for this is the contrast between the characteristic dimensions of the self-assembled structure and the film thickness causing relaxation of the film via the islands and holes [11].

2.1.3   Thermal Annealing

When a sample containing a non-equilibrium BCP film is exposed to heat of a suitable temperature for a long enough time, it increases the mobility of the film causing it to self-assemble in a way that is energetically favourable, i.e. to its equilibrium form [5]. This implies that the temperature has to exceed that of the glass transition temperature of the polymers in the BCP [5]. The increased mobility originates from decreased viscosity and increased diffusion as the temperature increases, but also through changes in the miscibility between the polymers in the BCP [5]. Published papers indicate that very little research into thermal annealing on PS-b-P4VP has been carried out. In the only article that was found, thermal annealing at 180°C was used jointly with SVA to self-align the BCP which resulted in a cylindrical microstructure [16]. Although this article does not show that thermal annealing alone can be used to obtain perpendicular cylindrical structures in PS-b-P4VP, it serves as an indication that PS-b-P4VP might be thermally annealed. Furthermore, since the temperature where the degradation of the blocks in PS-b-P4VP starts are quite high, ≈ 300°C for both PS and P4VP, degradation of the blocks should not pose problems during thermal annealing [17, 18]. However, since very little information exists on thermal annealing of PS-b-P4VP, the information in this section relies on research on PS-b-PMMA, which has been studied extensively [19].

For PS-b-PMMA, the needed processing time for thermal annealing to

result in a film that is in equilibrium follows an exponential law where a higher temperature requires significantly shorter annealing time [5]. However, at the decomposition temperature of any of the polymers in the BCP, the BCP film starts to degrade [13] meaning there is an upper limit to where thermal annealing can be carried out with a satisfactory result [13]. As mentioned before, since thermal annealing has to be carried out above the T_g of the polymers in the BCP, there is also a lower limit for thermal annealing [5].

One problem that arises when using thermal annealing is that it is hard to achieve structures that align perpendicular to the surface, especially for high χ-BCPs [19, 20]. Therefore, a few methods have been designed to circumvent this obstacle, one such method being to use a brush layer, which can be a random copolymer containing the blocks of the BCP in question, placed on the surface of the substrate underneath the BCP [19]. This reduces preferential wetting to the substrate, therefore, reducing the drive towards forming parallel structures [19]. Another similar approach is to use a top coat, which can reduce preferential wetting to the free air surface for one of the blocks which also reduces the drive towards parallel structures forming [20]. Yet another way is to use inorganic impurities to induce the formation of parallel structures during thermal annealing, this has been done with the block copolymer PS-b-P2VP [19, 21]. In this case, nanoparticles were mixed with the BCP, which induced a perpendicular structure of the PS-b-P2VP [21].

When comparing thermal annealing to SVA, there are benefits and drawbacks to each method. Generally, thermal annealing is simpler to carry out and is also cost-effective, indeed making it the more used method [13]. However, there are also clear drawbacks to using thermal annealing. One drawback of using thermal annealing instead of solvent vapour annealing is that it is distinctly harder to achieve perpendicular structures in a BCP film with thermal annealing and only a handful of block copolymers can achieve this without the use of brush layers, top coats, impurities or other similar ideas [19]. Another drawback is that for some block copolymers, the degradation temperature might be very close to, or under, the glass transition temperature T_g which makes thermal annealing very slow and therefore inefficient, or even impossible, thereby making SVA the preferred method of self-assembly in these cases [13].

2.2   Sequential Infiltration Synthesis (SIS)

Sequential infiltration synthesis (SIS) and Vapour phase infiltration (VPI) are collective names for techniques where precursors are infiltrated into a host material, for example a polymer, in which they interact with its functional groups [22]. With subsequent exposure to a co-reactant, a hybrid organic-inorganic material forms [23]. This cycle is typically repeated several times to facilitate a larger amount of infiltrated material [23].

SIS is typically performed in an atomic layer deposition (ALD) chamber, but with a modified pulse sequence [24]. The reason for this change is that in regular ALD film growth, the aim is to saturate all the reactive sites on the surface of the substrate to get a self-limiting reaction whereas, in SIS, the aim is to dissolve, diffuse and entrap the precursors inside of the BCP where the organic-inorganic material should form [24]. This essentially means that ALD is a surface process while SIS is a bulk process in which three-dimensional structures are obtained.

ALD is typically run at low precursor partial pressures while the partial pressures of the precursors in SIS needs to be significantly higher, to drive the precursor into the BCP film [24]. Apart from this, exposure times also needs to be increased in SIS because of the diffusion step where the precursors migrate into the BCP film [24]. In this thesis project, the precursors' trimethyl aluminium (TMA) and water vapour are used to form aluminium oxide, AlO_x [23].

There are a few different infiltration techniques that all belong to the SIS family since they are very similar in mechanism and only differ slightly in dosing sequence [22]. There is some confusion regarding the naming of these similar methods, but this report will use the nomenclature proposed by Leng and Losego for these [22].

The dosing sequence for the first method, named semi-static SIS consists of a static hold of the first precursor and after a set hold time, the chamber is evacuated to a vacuum [25]. After this, an inert carrier gas is added to the chamber to purge it [25]. Following this, the chamber is yet again brought to a vacuum after which the process is repeated, but with the other precursor [25]. When both precursors have been present in the chamber, one cycle is said to have taken place, after which, additional cycles are often performed [25].

The second method is referred to as either multiple pulsed infiltration (MPI) or flow mode SIS [22]. In this method, after a precursor has been

introduced into the chamber, the chamber is not purged to a vacuum to remove it, instead, a constant flow of an inert carrier gas is used to remove the precursors from the chamber [22]. The steps of MPI are summarised in the following paragraphs. Firstly, a precursor gas is introduced into the chamber for a set time, after which a hold step where no new precursor molecules are added to the chamber takes place [26]. During this step, an inert gas fills the chamber, eventually purging the chamber from the precursor[26]. After this is achieved, the co-reactant is added to the chamber following the same steps as the first precursor [26]. After these steps have been performed, one cycle is completed, after which consecutive cycles can follow [26].

The third method highlighted by Leng and Losego is referred to as sequential vapour infiltration (SVI) [22]. This differentiates from the semi-static SIS and MPI since it delivers multiple doses of the same precursor before the reactant is introduced into the chamber, often referred to as a soak step [22, 27]. Following this soaking step, a carrier gas is typically used to purge the chamber of the precursor, after which the co-reactant is introduced to the chamber in multiple doses [27].

2.2.1 SIS Mechanism

The mechanism that describes how the precursors form their bond to the polymer is known as a Lewis acid-base interaction [23, 24]. The metal-organic precursor behaves as a Lewis acid and the functional groups in the polar block of the BCP act as a Lewis base [23, 24]. Initially, most of the research on the SIS mechanism was done on PS-b-PMMA [24]. However, research into the interactions taking place on the BCP PS-b-P2VP, which is very similar to the BCP PS-b-P4VP used in this thesis project, has since been conducted [23]. Therefore, this background will delve deeper into the interactions relevant for this specific polymer mostly.

In general, the SIS mechanism can be described using a three-step process, sorption of the precursor gases into the BCP, diffusion of the precursors in the BCP and entrapment of the precursors within the BCP [22]. For the BCP PS-b-P2VP, and therefore likely also PS-b-P4VP, the most important steps are precursor diffusion and precursor entrapment [23].

During the diffusion step, precursors diffuse into the polymer film, where they can form a coordinative bond with the polymer moieties [23]. The depth of the diffusion of the precursors into the polymer is time-dependent and infiltration times should be carefully considered as an insufficient dif-

fusion time can result in only a shallow layer of infiltrated material close to the surface forming [24, 28]. The coordinative bond formed between the precursors and the pyridine moieties is reversible meaning both forward and reverse reactions take place which affects the concentration of bound and unbound precursors in the system [23]. The rate of these reactions is temperature dependant forming three temperature regions; the low-temperature region, the balance point (BP) and the high-temperature region [23]. At the low-temperature region, the forward reaction is favoured meaning the concentration of bound precursors is higher than that of unbound, whereas in the high-temperature region the reverse reaction is favoured and the concentration of unbound precursors is greater [23]. At the balance point, these reactions are equal, meaning the concentration of bound and unbound precursors at equilibrium will also be equal [23]. It was shown by Weisbord et al. that the precursor molecules ability to attach and detach from polymer moieties is equally important and that at the balance point, the mass gained from infiltration is the largest [23]. The reason for this is that when the forward reaction is favoured, the diffused precursors bind strongly at the top of the film, thereby hindering additional precursors to diffuse deeper into the film resulting in lower mass gain [23]. Moreover, when the reverse reaction is favoured, limited amounts of coordinatively bonded precursors result in a lower mass uptake even though deeper diffusion is achieved here [23]. Meanwhile, at the balance point, the constant rate of the forward and reverse reaction allows precursors to detach from a pyridine moiety and diffuse further down into the polymer film, while the amount of coordinatively bound precursor is sufficient to allow for a high amount of mass gain [23]. The balance point for PS-b-P2VP is rather high compared to other BCPs, 210°C [23]. The reason for this is the pyridine group in P2VP, which is a strong Lewis base [23, 29]. Since PS-b-P4VP also contains a pyridine group, it can be assumed to be close to that of PS-b-P2VP [29]. In a slower reaction, the coordinatively bound precursors are transformed into covalent and non-reversible bonds, in the case of TMA infiltration Al-O bonds, as long as there is enough activation energy for the bond to form [24, 23]. Subsequent exposure to the co-reactant, water vapour, causes oxidation of the covalently bonded precursors forming O-Al-OH species when TMA is the precursor used [23]. Furthermore, these oxidised species serve as reaction sites for the subsequent infiltration cycles [24, 12]. Notably, when the non-reversible bonds have formed, the BCP structure is effectively locked in place, meaning it can withstand higher temperatures while still retaining the microphase separated

13

pattern [23].

2.2.2 SIS and Block Copolymers

The combination of block copolymers and SIS is interesting because of the possibility to infiltrate an inorganic material into only one of the blocks [24]. This can be achieved when one of the blocks lack polar groups, for example, polystyrene, which prevents interactions between the polymer block and the diffusing precursors [24]. Instead, the non-polar polymer block can act as a diffusive channel for the precursors to the reactive sites in the polar polymer block [24]. By utilising this, an etch mask made of a metal oxide containing the pattern of the BCP:s can be created [12]. Since these etch masks contain heavier elements than polymers typically do, it typically yields a higher etch resistance than when only using the BCP:s by themselves [30]. This means SIS on BCPs combined with etching is an effective way to transfer a BCP pattern into a silicon wafer [30].

2.3 Reactive Ion Etching

In reactive ion etching (RIE), a combination of physical and chemical processes are utilised to etch away atoms from the surface of a substrate in a low pressure chamber [14]. Although both physical and chemical processes are active, the dominant etching phenomenon in RIE is chemical, through reactive and corrosive gases [14]. In a RIE process, the selected gasses are introduced into the vacuum chamber after which free electrons present in the chamber are accelerated by a radio frequency (RF) field, causing these electrons to acquire enough kinetic energy to ionise the injected gas molecules upon collision [14]. Through this process, more free electrons become available causing ionisation of even more gas molecules quickly leading to a large amount of available ions and free electrons [14]. In a RIE with a configuration of planar electrodes, the RF power source is connected to one electrode, the cathode, while the other electrode is grounded, the anode [14]. The free electrons that resonate in the chamber due to the RF field causes the electrodes to charge up negatively due to the fact that the free electrons move faster than the ions [14]. Since the cathode is not connected to ground, it will become more negatively charged than the anode, which, in turn, will cause ions to be accelerated towards the cathode [14]. This ion bombardment affects the sample by physical ion sputtering. The chemical processes, that are the

dominant etching processes, affect the sample in a few ways [14]. If the ions are reactive species, the can react with the surface atoms directly by forming volatile compounds, thus leaving the substrate [14]. The ions can also cause absorbed gas molecules on the substrate surface to dissociate, producing radicals which reacts with the surface atoms forming volatile compounds that escape the surface [14].

As mentioned before, increased RF power leads to increased ion bombardment of the sample, due to the higher self-biasing voltage of the sample, which is not always desired [14]. In inductively coupled plasma reactive ion etching (ICP-RIE), which was used in the Master's thesis project, the plasma generation is separated from the etching chamber which allows the RF power and self-biasing voltage to be independently controlled [14]. This is important as it can affect the etching selectivity which is the ratio of the etching rate for the substrate versus the etching rate of the mask [14]. During etching, it is often desired that the exact dimension of the mask pattern is transferred to the substrate, however, in practice there are always distortions and lateral etching taking place [14]. Etch anisotropy is a measure of how much lateral etching has occurred, where isotropic etching means identical etching rate in all directions whereas anisotropic etching includes no lateral etching [14]. One way highly anisotropic etching conditions can be achieved for silicon etching is by introducing the gas SF_6 combined with C_4F_8 into the chamber [31, 32]. The reason this achieves highly anisotropic etching is because the C_4F_8 forms a passivation layer, inhibiting the SF_6 from etching except at the bottom where the ion bombardment removes the passivation film [31, 32].

2.4   Nanoimprint Lithography

In nanoimprint lithography, a template containing a specific pattern, referred to as a stamp, is used to mechanically transfer a pattern to a polymer film [33, 34]. The NIL process is performed at a temperature above the T_g of the polymer film, allowing it to shape itself after the pattern on the stamp when pressure is applied to the polymer film. After the polymer film has been displaced by the stamp, it is hardened through a curing process. There are multiple ways this is can done. One method used is to cool the polymer film down below the T_g before removing the pressure and demoulding the polymer film from the stamp, which is referred to as thermal NIL [33]. Another method is to utilise UV-light to cure the polymer film, which is referred to as

UV-NIL [33, 35]. Using these processes, sub-10 nm resolution is attainable in a high-throughput fashion at a relatively low-cost [33]. Since the stamp is used as a template, its defects will be carried forward into the polymer film, meaning the choice of patterning technique used for stamp manufacturing is of great importance. One method utilised to manufacture a NIL stamp is to use electron beam lithography (EBL) where an electron resist, for example PMMA, is exposed to an electron beam that is scanned across the surface [36, 37]. After resist development a metal layer can be evaporated onto the developed resist and following lift-off of the resist, a pattern is present on the sample [36, 37]. After subsequent etching, a silicon NIL stamp has been manufactured [36, 37]. To facilitate removal of the polymer film after imprint, a NIL stamp is often treated for anti-sticking by depositing a monolayer of fluor-containing molecules using chemical vapour deposition [36]. In this Master's thesis project, self-assembly of a BCP film combined with infiltration of aluminium into the film and subsequent etching is used to create the NIL stamp. A schematic of how this NIL stamp then was used to manufacture the polymer film where the anti-bacterial measurements took place, which was the motivation for this Master's thesis project, is presented in Figure 3.
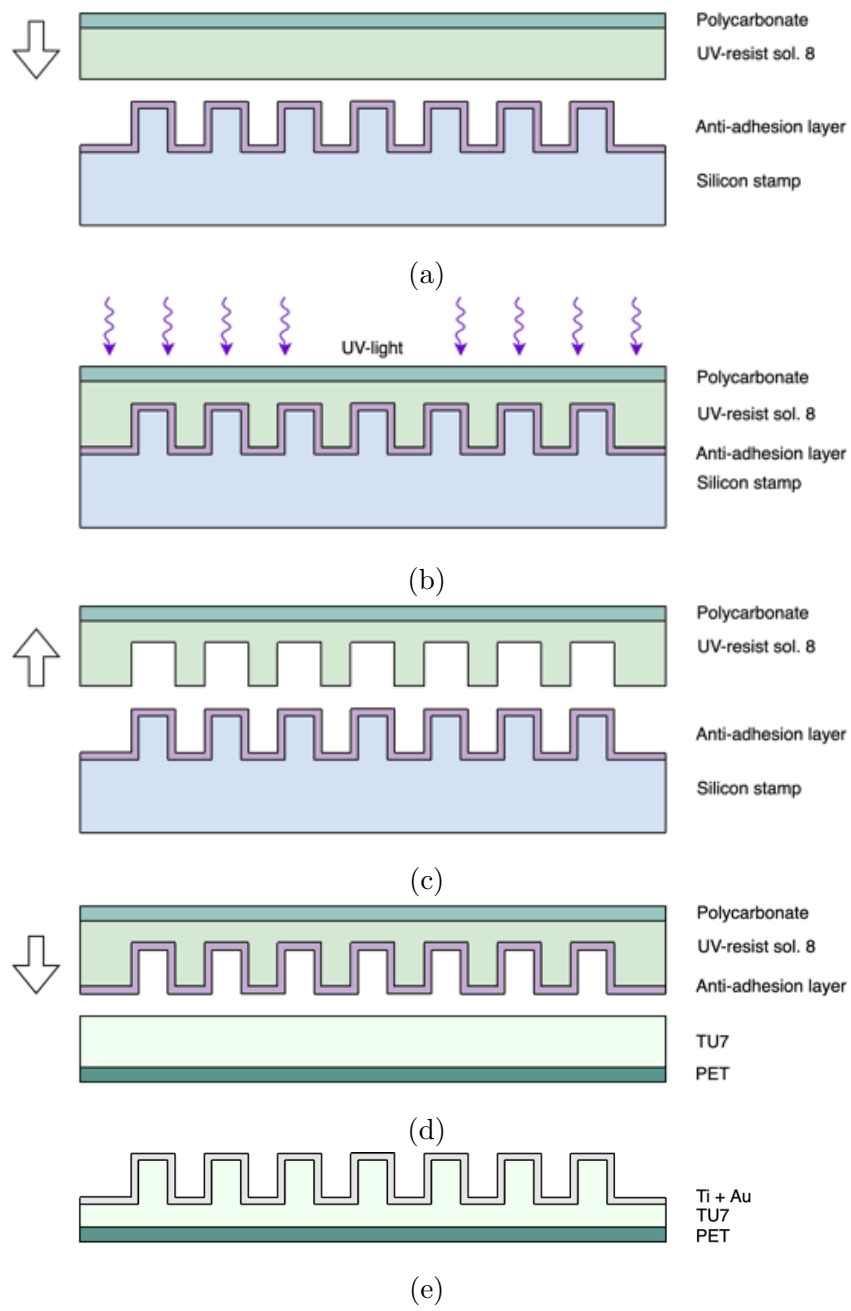
Figure 3: Schematic of the NIL processing steps to obtain the polymer film where the anti-bacterial measurements were performed, starting from the the silicon stamp.

17

In the first processing step, see Figure 3a, the silicon NIL stamp with an anti-adhesion layer and a two-layered polymer film of UV-resist 'solution 8' and polycarbonate are loaded into the NIL tool. In the second step, 3b, the NIL stamp and the polymer film are brought into contact and UV-light is used to cure the UV-resist layer. The third step, 3c, shows the patterned polymer film removed from the silicon stamp. This film is subsequently given an anti-adhesion layer before proceeding to the next step. In 3d, the patterned film is then seen being utilised as a stamp for pattern transfer into another polymer film with one layer of 'TU7' on PET. The last step, 3e, shows the finished TU7/PET film after it has been coated with titanium and gold. A more in-depth description of these processing steps can be found in Appendix C.

2.5   Antibacterial Properties

To be able to manufacture a silicon stamp for nanoimprint lithography that contains a pattern that makes a polymer film antibacterial, it is important to understand what features are responsible for this effect. An important scientific article in this field is by Ivanova et al. who found that the surface of cicada wings acts as a natural bactericidal surface [38]. The reason for this bactericidal effect was found to be a nanopattern located on the cicada wings' surface, a structured array of nanopillars. These pillars caused cell penetration, resulting in the death of the bacterial cells. In a subsequent review article, multiple micro- and nanostructures causing bacterial cell death are reviewed [39]. The antibacterial structure this thesis project aims to pattern is an array of rigid pillars on the nanoscale. The way this can kill bacterial cells is through suspension of the membranes of these cells on the pillar array, which leads to stretching of the membrane beyond the elastic limit, thus killing the cells [39]. This bactericidal effect has been found for nanopillar structures in a height range of 100-900 nm, a width range of 20-207 nm and a spacing distance of 9-380 nm [40]. Hence, these were the interesting parameter ranges to optimise for during processing.

18

3 Experimental

The block-copolymer used in this project was PS-b-P4VP from Polymer Source, Inc., Canada [41]. The molecular weights of the blocks used were $M_n = 50000$ g·mol^{-1} for PS and $M_n = 17000$ g·mol^{-1} for P4VP. The glass transition temperature is $T_g = 103°$C for the PS block and $T_g = 145°$C for the P4VP block [41].

The tool used for infiltration of the BCP was a Veeco Savannah 100, formerly of Cambridge NanoTech. The recipe utilised can be seen in full in Table 3 of Appendix A, but the most important parts are described in the following paragraphs. TMA and water vapour were utilised as precursors with infiltration temperatures of 90, 100, 145 and 200°C. The pulse duration of the TMA was 15 ms, repeated after 0.8 s a total of 100 times, followed by a purging time of 90 s to remove the TMA from the chamber. Subsequently, water vapour was introduced into the chamber with a pulse duration of 10 ms repeated after 0.8 s a total of 50 times, followed by a purging time of 600 s to remove the water vapour from the chamber. This completed one cycle, and during the project, infiltration was tested for one, four and eight cycles.

An ellipsometer was employed to measure film thicknesses. This system was a Woollam RC2 variable angle spectroscopic ellipsometer [42]. The collecting angle was varied from 55 to 70 degrees and the wavelength range used was between 400 to 1000 nm.

An inductively coupled plasma reactive ion etcher (ICP-RIE) was used for polymer ashing as well as for the etching with the alumina etch mask. This machine is called the APEX SLR ICP manufactured by Plasma-Therm. The recipes used during ashing and etching can be found in their entirety in Table 4 and 5 of Appendix B, but the most important part are described in the following paragraphs. For the polymer ashing, the gas in the chamber was O_2, the radio frequency field was set at 25 W and the inductively coupled plasma was set at 10 W. For the etching, SF_6, C_4F_8 and Ar were present in the chamber with the radio frequency set at 25 W and the inductively coupled plasma set at 300 W.

The Hitachi UHR SU8010 FE-SEM was used for all cross-sectional SEM micrographs as well as some of the top-view SEM images. Apart from this, the Zeiss Gemini 500 FE-SEM was used for much of the top view imaging. Both of these instruments utilise a field emission gun for emitting the electrons in the beam.

4 Results and Discussion

The first part of this Master's thesis project consisted of finding optimal parameters for the SIS processing. After studying the literature on SIS, the temperature was chosen as the parameter to optimise due to its considerable effect on mass gain during infiltration as mentioned in Section 2.2.1.

4.1 Sequential Infiltration Synthesis

From an earlier try on PS-b-P4VP by Anette Löfstrand, reasonable parameters where infiltration occurs were already known [43]. The temperature used by her was 90°C. However, it was mentioned in the paragraph about the balance point in the background, Section 2.2.1, that the infiltration is the largest at 210°C for the very similar PS-b-P2VP. It is therefore reasonable to investigate how higher temperatures affect infiltration in PS-b-P4VP.

Since the glass transition temperature, T_g, is 103°C for the PS block and 147°C for the P4VP block, it is interesting to examine the highest possible temperatures under these T_g-temperatures in case polymer flow of one or both polymers affect the results. The four temperatures used for infiltration are therefore chosen as 90, 100, 145 and 200°C.

In the following sections, the results after each stage of processing are presented.

4.1.1 Solvent Vapour Annealing

After the samples had been exposed to the solvent vapour annealing treatment, they were analysed with an ellipsometer. This was done to obtain the thickness of the BCP film, which was measured to 28 nm ±2 nm. Apart from this, inspection of the film using an SEM was conducted, the result of which can be seen in Figure 4.
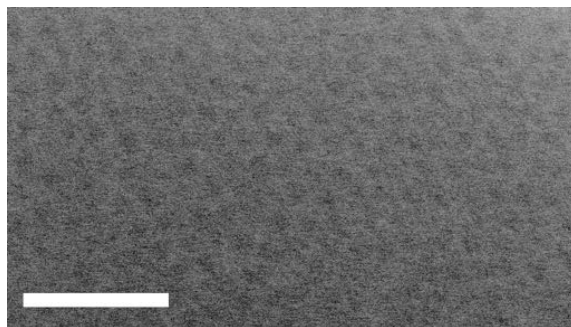
Figure 4: SEM image of the microphase separated BCP after solvent vapour annealing. The P4VP blocks show up as dark circles while the PS matrix is seen as the whiter parts in the surrounding. The scale bar is 250 nm.

It is visible that a microphase separated structure has formed with cylinders discernibly due to their somewhat darker shade as compared to the matrix. These darker cylinders consist of P4VP and the matrix of PS.

4.1.2 Infiltration

After the samples were exposed to the precursors in the ALD tool, to form infiltrated AlO_x, they were analysed in an SEM. The following images were captured immediately after infiltration, before any other processing.
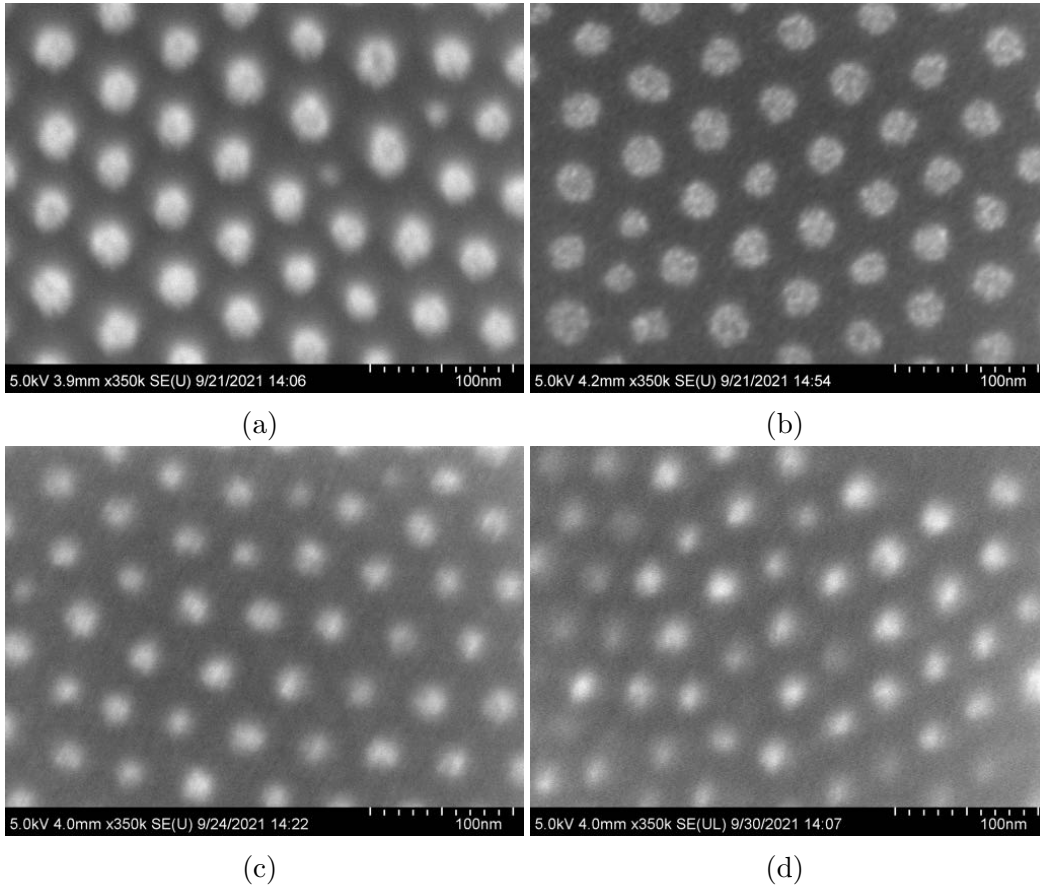
Figure 5: SEM images of the samples from above. The samples were processed at 90, 100, 145 and 200°C in increasing order from a to d. Notice the decrease of the apparent diameter of the cylinders as the temperature increases. Data on this can be seen in Table 1.

Based on these images alone, it is possible to speculate on both the pattern transfer quality and the amount of infiltrated AlO_x infiltrated into the cylinders. Regarding the pattern, it appears that the pattern from the BCP film has been transferred to the hybrid organic-inorganic material for all samples. However, for the higher temperature sample, the cylinders seem to have a smaller diameter and the border between the two blocks appears more blurry. Since the quality of pattern transfer is of utmost importance, the lower temperatures seem favourable for the application, even though the samples infiltrated at 145 and 200°C could potentially contain more alumina.

Although, this remains to be seen as removal of the polymer film might paint a different picture. If the diameter of the cylinders of infiltrated alumina is smaller, this will be contrary to the findings of Weisbord et al. which state that the infiltrated mass should increase with higher temperature in this temperature range mentioned in Section 2.2.1. Apart from this, it is also evident that the infiltrated alumina is not homogeneously distributed in the P4VP, most notable in Figure 5b but likely present in all four samples. See Figure 5b where islands of higher contrast are visible inside the P4VP cylinders. This might indicate that four cycles of infiltration are not sufficient or it might be some other parameter that needs fine-tuning later on. If this heterogeneity will pose a problem when the alumina is used as an etch mask remains to be seen though. It is also unclear how these islands of alumina in the P4VP cylinders are affected by the ashing of the BCP. Therefore, it is relevant to image the samples infiltrated at 145 and 200°C again after the ashing step is conducted.

An interesting observation is that for the sample processed at 200°C, significant flow occurred on the micro-scale while the cylindrical pattern was still retained on the nanoscale. This is presented in Figure 6.

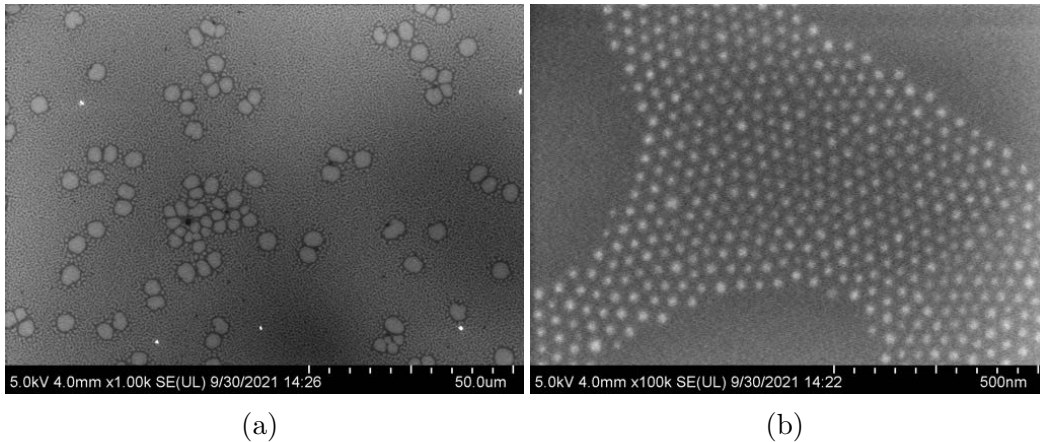(a)   (b)

Figure 6: SEM image of the sample processed at 200°C where significant flow is visible, notice the micrometer sized circles that have formed, in a) while the nano scale cylindrical pattern is retained, shown in b).

This finding is interesting as it suggests that it might be possible to carry out thermal annealing while the sample is in the ALD chamber during

SIS infiltration. Although, of importance is that the microphase separated structure of perpendicular cylinders was present before the annealing since SVA was carried out beforehand, but importantly, this structure was not destroyed by the thermal treatment. If thermal annealing inside of the ALD tool could be performed in a way that creates good self-assembly of the BCP film, multiple hours of processing time could be saved by minimising the number of processing steps.

However, in this sample there were large areas that formed with no cylinders present, resulting in large areas of the sample that contained no structures. This means that the thermal annealing in the ALD chamber has to be improved, likely by increasing the thickness of the BCP film, to obtain samples usable for the application of this Master's thesis project. Furthermore, as samples the size of a square centimetre or more was be needed, this approach might be unsuccessful. More research was carried out to determine whether this is a viable approach or not.

To obtain information about how the thickness of the BCP film was affected, ellipsometry was used. The thicknesses presented for the different samples are a mean of three data points and can be seen in Table 1.

Table 1: The measured thickness of the BCP film and the average diameter (of 10 cylinders) after infiltration of AlO_x for the different samples infiltrated at the temperatures 90, 100, 145 and 200°C. The thickness of the BCP film for the samples before infiltration was 28 nm.

	BCP film thickness			
Processing temperature (°C)	90	100	145	200
Thickness (nm)	25	24	29	32
Average diameter (nm)	24	25	19	16

In the data presented in Table 1, a trend where film thickness rises as the processing temperature increases is noticeable. This fits in well with the assumption that the balance point for PS-b-P4VP is close to that of PS-

24

b-P2VP at 210°C [23] since a thicker BCP film after infiltration suggests a higher amount of infiltration. However, the diameter of the cylinders appeared to be smaller for the samples infiltrated at 145 and 200°C in Figure 5 which might indicate that at higher temperatures the infiltration occurs but that the mass gain affects the height instead of the width of the cylinders. More information is needed to draw any conclusions.

4.1.3   Polymer Ashing

After the samples were exposed to the oxygen plasma in the APEX SLR F-based RIE, where the uninfiltrated part of the BCP film was removed, they were analysed in an SEM microscope. The following images, see Figure 7 were captured immediately after 150 seconds of polymer ashing, before any other processing.
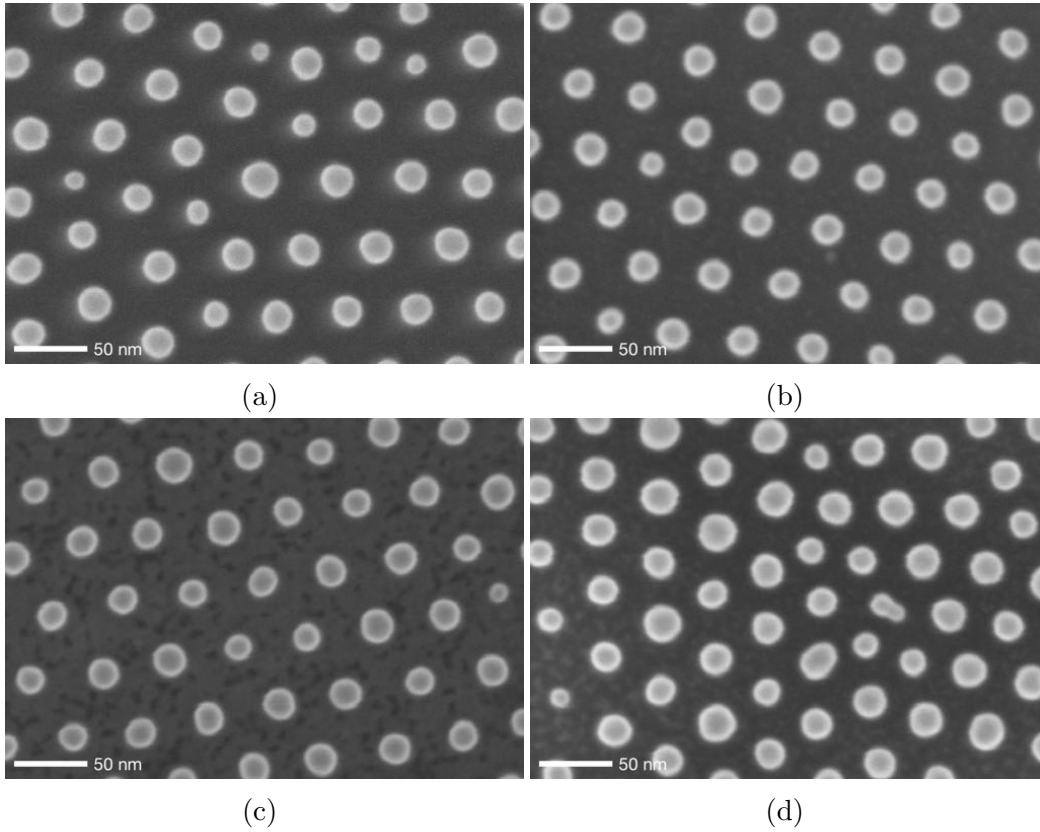
(a)　　　　　　　　　　　　(b)

(c)　　　　　　　　　　　　(d)

Figure 7: SEM images of the samples from above after SIS and polymer ashing. The samples were processed at 90, 100, 145 and 200°C in increasing order from a to d. Notice that the observed blurriness at the borders of the cylinders for the samples processed at higher temperatures has vanished.

From these images, one can conclude that the quality of the pattern transfer does not seem to be affected by the different temperatures. Furthermore, the trend where the diameter decreased with increasing temperature is no longer evident, which can be seen when the average diameter of these samples were calculated, see Table 2. This might have been the result of the different heights of the polymer film after infiltration, essentially covering the top of the cylinders containing alumina with PS more at higher temperatures, but this is simply speculation. After these images, cross-sectional SEM micrographs were also captured to observe the shape of the structure.
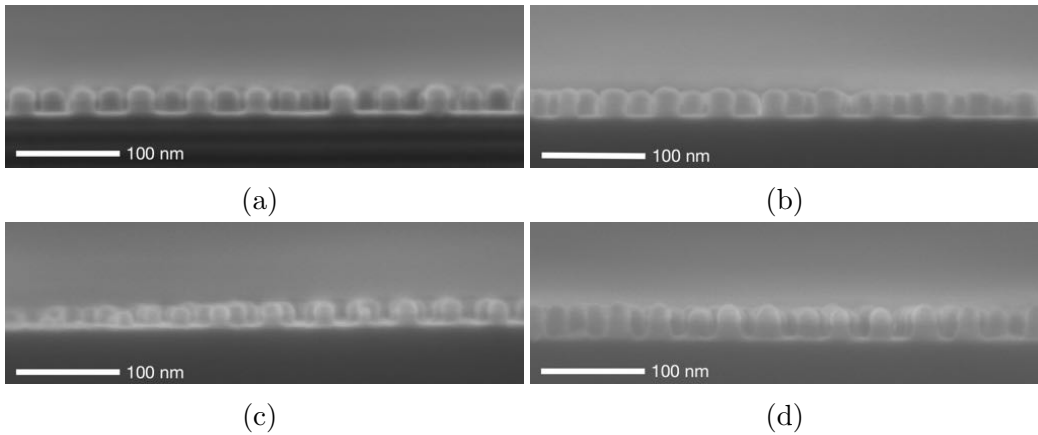
Figure 8: SEM images of the samples in cross section after SIS and polymer ashing. The samples were processed at 90, 100, 145 and 200°C in increasing order from a to d.

From the cross-sectional images captured, the height, width and aspect ratio of the cylinders for the different samples were measured and calculated. Notice that in Figure 8, some of the cylinders have a shape similar to a mushroom, most notable in Figure 8d. This means the width is dependent on at what height on the sample it is measured. However, as the largest width is easiest to measure, this width is presented. The information gathered is shown in Table 2. It is worth mentioning that during the entirety of the Master's thesis project, multiple samples were infiltrated at the temperatures 90, 100, 145 and 200°C with very similar results, pointing to a reproducibility of the results obtained in this report.

Table 2: The measured height and the largest width was averaged for 10 cylinders in the different samples. Apart from this, the aspect ratios of said cylinders were also calculated.

	Cylinder measurements			
Infiltration temperature (°C)	90	100	145	200
Height (nm)	25	27	24	32
Width (nm) (largest)	20	20	21	21
Aspect ratio (Width:height)	1:1.25	1:1.35	1:1.14	1:1.52

There are a few notable things to mention regarding these measurements. Drift in the vertical direction during SEM imaging impacts the reliability of the height measurement, which in turn gives the aspect ratio a value that is somewhat unreliable. Although there seems to be a trend where higher infiltration temperature relates to greater height, the measurement error due to the vertical drift, as well as the inherent measurement error of the SEM, means it is not possible to directly say if this trend is accurate. Notably, the sample processed at 145°C does not conform to this trend. One other possibility is that the sample infiltrated at 200°C differs from the other three samples as the average height of its cylinders were 5 nm more than the second tallest sample's cylinders. Since flow of the BCP film only occurred for this sample, this is interpretation is not far fetched, but to be certain, further investigation is needed. The reason these measurements are of interest is because a thicker etch mask could potentially transfer to a higher aspect ratio of the etched structures. Therefore, etching was used to investigate how well the cylinders in the different samples held up, giving information about which infiltration temperature is optimal to use. The etching time used was four minutes and thirty seconds as etching results from an initial sample indicated that the etch rate in silicon is around 17 nm per minute. Hence, an etching time of 4.5 minutes should result in a pillar height of approximately 75 nm plus the remaining etch mask, rendering an aspect ratio of the pillars of around 1:3.

One other notable thing is the apparent mushroom shape of the cylinders.

This shape may likely form because AlO_x acts as places where additional precursors can bind onto, similarly to the P4VP functional groups, as mentioned in the background. Furthermore, as the P4VP is transformed into a hybrid organic-inorganic material, diffusion of precursors through it might be affected, which could result in a majority of the added AlO_x being close to the top of the cylinders.

4.1.4 Etching

As mentioned earlier, an etching time of 4.5 minutes was used at this stage. When the etching of the samples infiltrated at the different temperatures was done, cross-sectional SEM images were captured to see if there was any difference in terms of etch selectivity between the alumina masks and the silicon substrate. These images are presented in Figure 9 below.

(a)   (b)

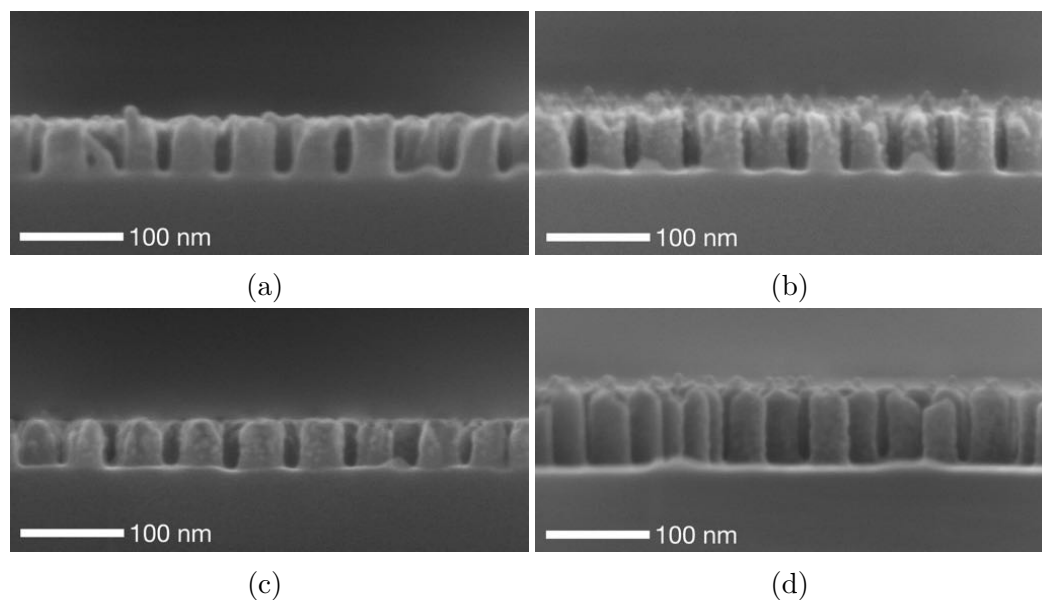(c)   (d)

Figure 9: SEM images in cross section of the samples after etching for 270 s. The samples were processed at 90, 100, 145 and 200°C in increasing order from a to d.

Judging by the images, the etching is highly anisotropic since the sidewalls have nearly no positive incline. Notably, the uppermost part of most of the cylinders appears rough. This is likely due to over-etching of the samples

29

since there is no visible interface between the silicon and the AlO_x mask in any of the samples. This was the case at even higher secondary electron suppression detection where most of the image was formed by backscattered electrons, which is more sensitive to the atomic number of the sample. Furthermore, since the aspect ratio is far from 1:3 in any of the samples, it is reasonable to assume the etch mask has been removed in all of the samples. However, of great interest is the finding that the sample infiltrated at 200°C held up to the etching significantly better than the other samples. This supports the interpretation of the cross-sectional SEM images mentioned in Section 4.1.3 that the sample infiltrated at 200°C differentiates from the other ones. Due to the balance point, it was expected that the aspect ratio of the samples would increase with increasing infiltration temperature. This trend is not clear in the figure above, except for said sample infiltrated at 200°C which showed a substantially larger aspect ratio. The reason this trend is not seen for the other samples might be due to the over-etching, which makes the top of the cylinder uneven and thus makes the height hard to measure. Therefore, it is not possible to say anything about the difference in aspect ratio for the samples processed at 90, 100 and 145°C as the differences are well within the error margin. A graph of this can be seen in Figure 10
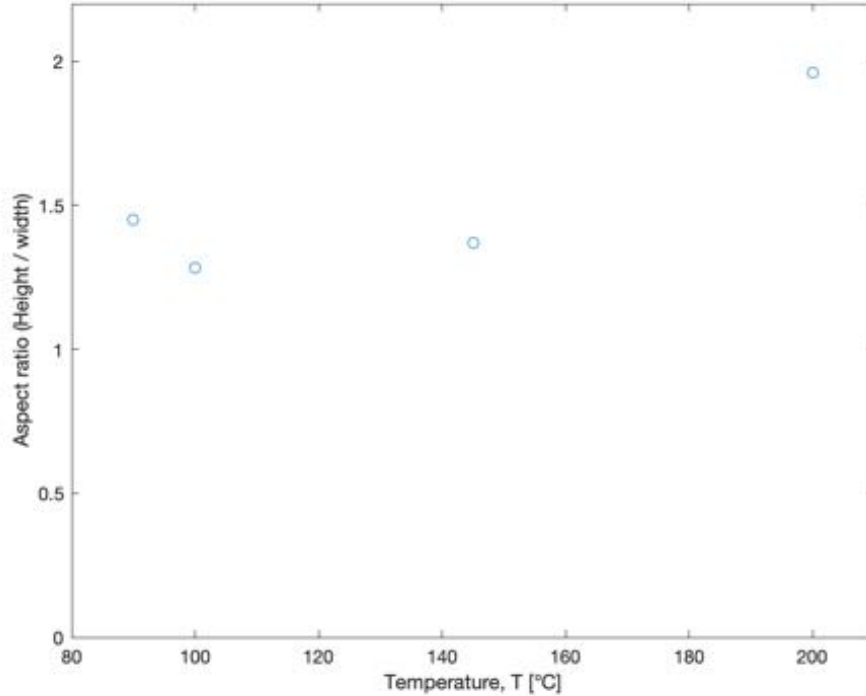
Figure 10: The aspect ratio for the different infiltration tempera-
tures measured from the images in Figure 8. Note that the samples
infiltrated at 90, 100 and 145°C did not affect the SVA-induced self-
assembly, while the sample infiltrated at 200°C did.

From the conclusions drawn by the information in Figure 9 and 10, two
questions arise. What is the highest aspect ratio achievable using this method
without affecting the SVA-induced self-assembly? How long is it possible
to etch before the etch mask is exhausted if more cycles are used during
infiltration, which similarly to the sample infiltrated at 200°C should result
in more alumina infiltrated. Additional experiments were performed that
answers these questions, presented below and in Section 4.3.

A new sample was infiltrated at 90°C, the infiltration temperature that re-
sulted in the best etch mask (although within the error margins) for the three
infiltration temperatures that did not affect the SVA-induced self-assembly,
see Figure 10. This sample was split into four parts which were etched for
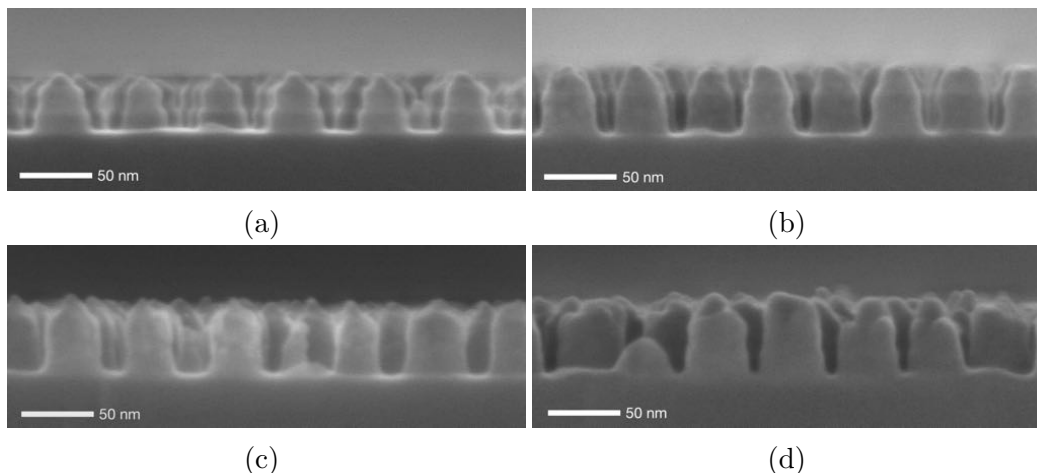50, 100, 150 and 200 seconds respectively. The results can be seen in the

figure below.

Figure 11: SEM images in cross section of the etch rate sample infiltrated at 90°C. The samples were etched for 50, 100, 150 and 200 seconds in increasing order from a) to d). Notice the interface of silicon and the etch mask which is visible as a contrast difference in image a) and b).

In Figure 11, the progression of the etching process can be seen. An interface between the etch mask and the silicon is visible in 11a and 11b but not in the other two images. This provides information about the optimal etching time at 90°C, which should between 100 and 150 seconds if the etch mask is to be etched away completely.

4.2 Thermal Annealing

After the initial results of the infiltration at 200°C were obtained, shown in Figure 6, additional experiments were carried out to check the validity of using thermal annealing in place of solvent vapour annealing to direct the self-assembly of the BCP film. The reason this was examined was the possibility to reduce the processing time if self-assembly could be induced while the sample was in the ALD chamber. A sample with a 26 nm thick BCP film that had not been subject to SVA was placed in an ALD chamber heated to 150°C. When the sample was loaded, the temperature was elevated to 200°C, an increase that took approximately 15 minutes, after which the

SIS infiltration took place. The infiltration procedure was carried out for 71.7 minutes, meaning the sample was exposed to temperatures above T_g of both polymer blocks close to 87 minutes. Notice however that the shape of the BCP film begins to lock into place after the hybrid organic-inorganic network starts to form, as mentioned in section 2.2.2. This effectively minimises the time thermal annealing can take place. After the thermal annealing and infiltration, the uninfiltrated parts of the BCP film was removed by O_2 polymer ashing to make the infiltrated spots easy to distinguish. The ashing was carried out for 150 seconds. The images captured afterwards are presented in the figure below.
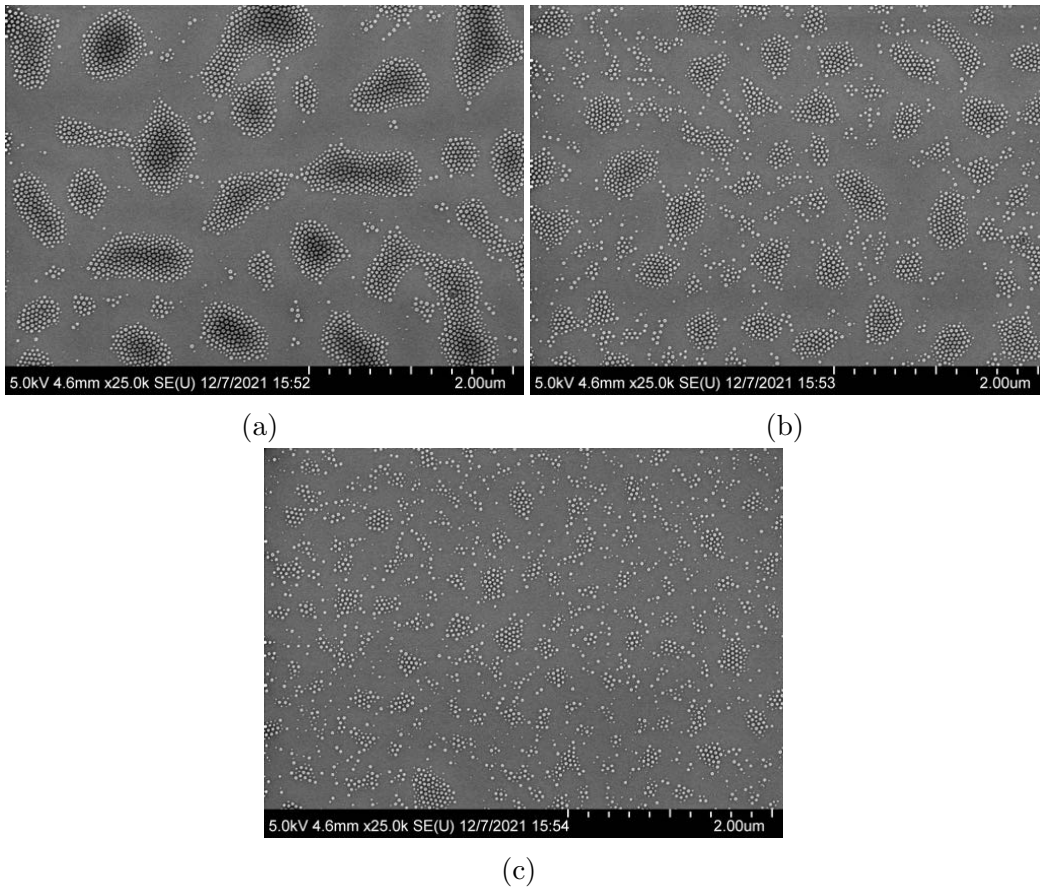
Figure 12: SEM images of the sample used for the thermal annealing experiment. Notice the increased disorder from image a) to c). This increased disorder was seen when moving from the edges, a), into the middle of the sample, c).
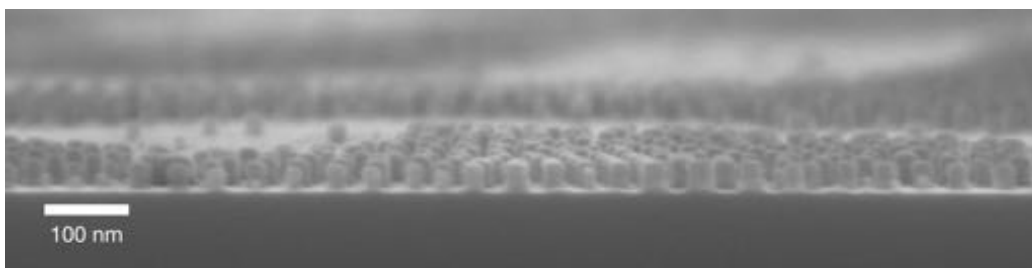
Figure 13: Cross section SEM image with 5° tilt captured after polymer ashing of the cylindrical AlO_x of structures formed during thermal annealing and infiltration. This image was captured closer to the edge of the sample where the coverage of cylinders was better.

From Figure 12 and 13 it is visible that vertically aligned cylinders have been created. Remember that this sample did not have any solvent vapour annealing performed beforehand. Therefore, it is certain that thermal annealing can be used to induce the PS-b-P4VP BCP film to rearrange into a self-assembled shape. Furthermore, it is observed that the best cylinder coverage was seen at the edges of the sample. As the electron microscope was used to image closer and closer to the centre of the sample, the order of the cylinders gradually diminished. This is evident when comparing Figure 12a, 12b and 12c with each other. This adverse effect is likely due to the low initial thickness of the film, as the initial film thickness can be expected to be somewhat heterogeneous after spin coating with a greater thickness closer to the edges. Furthermore, this is also validated by the samples that were solvent vapour annealed that also had areas with significantly lower coverage of cylinders due to the low initial thickness of the BCP film. The difference in these cases though is that the SVA processed samples had nearly no cylinders where the coverage was low and high order everywhere else, while the cylinders subjected to thermal annealing just gradually decreased in coverage closer to the centre. Apart from this effect, the homogeneity in cylinder size is also of interest. To control this, a high magnification image was captured and then analysed using the ImageJ software. This image is presented in Figure 14a.
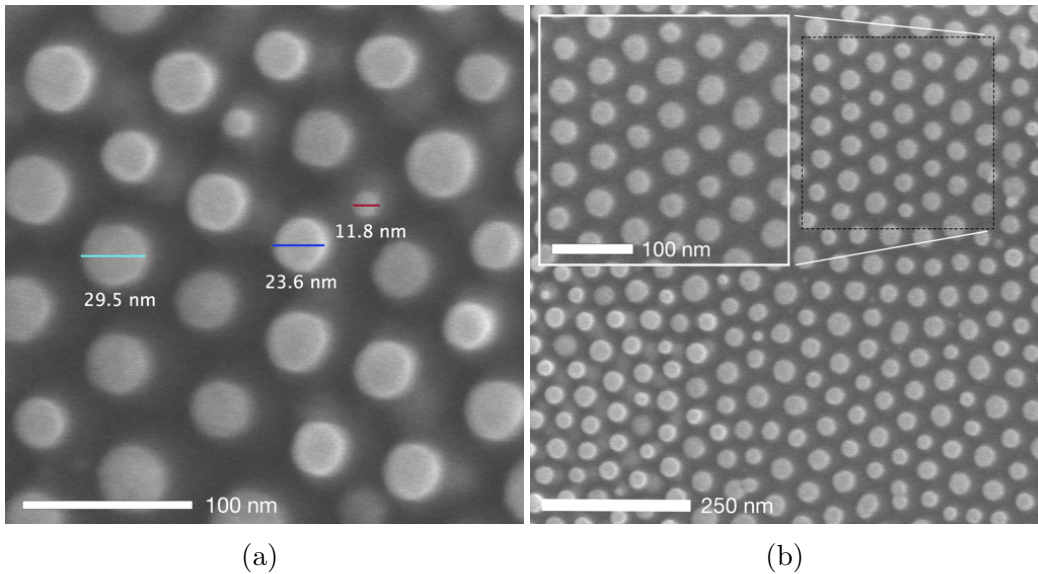
Figure 14: SEM image captured after polymer ashing of a sample used for the thermal annealing investigation. a) Notice that the size of the cylinders vary markedly with the largest having a diameter of 29.5 nm and the smallest a diameter of only 11.8 nm. b) Observe the local hexagonal ordering of the cylinders in the top left corner as well as the cloudiness of the background between the cylinders located in the bottom left corner.

In Figure 14b, what appears as white shadows in proximity to some of the cylinders are visible. This could possibly be the result of infiltration starting before the thermal annealing had finished the microphase separation reconstruction and thus infiltrating some alumina into places that contained P4VP before the microphase separation was finished. It would be interesting to give the thermal annealing more time before infiltration starts to see if this effect will disappear. Furthermore, locally hexagonally placed cylinders are highlighted. Although this is limited to an area of around 200 nm^2, it provides information about the possibility of achieving ordering of the cylinders formed during microphase separation with thermal annealing and deserves further study. From Figure 14a, it is also definite that the thermal annealing processing has resulted in the large size distribution of the formed cylinders in regards to diameter. The largest measured cylinder had a diameter of 29.5 nm while the smallest had a diameter of only 11.8 nm. As it is imperative

that the cylinders are similar in shape for etching to work properly, since they make up the AlO_x etch mask, thermal annealing might not be suitable to use in this project. Furthermore, long-range order and film coverage is important for the application of the samples created during this project, meaning additional experiments would have to be carried out before this technique is advisable to use for the processing. However, the thermal annealing process could likely be optimised considerably, resulting in better structures in regards to size distribution and coverage. Two possible parameters to experiment with is trying thicker BCP films which would allow for a better film coverage and longer thermal annealing before infiltration occurs which would allow the BCP film to rearrange for a longer time before it is locked in place by the alumina. This may result in cylinders without the white shadows apparent in Figure 14a.

4.3   Reactive Ion Etching

By knowing the height of the etch mask cylinders in a sample, the etch rate of the etch mask and the silicon can be obtained. By first etching for a short time, for example, 90 seconds, and then measuring the height of the remaining AlO_x part of the cylinders as well as the depth from the interface of etch mask and silicon to the bottom of the cylinders. This was done on a sample infiltrated with eight cycles of TMA and H_2O at 90°C. The images captured are presented below.
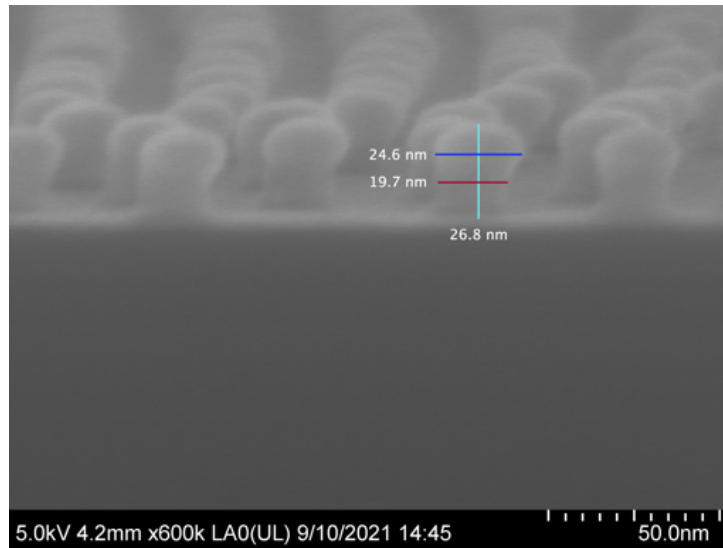
Figure 15: SEM images of the cylindrical AlO$_x$ structures before silicon etching. Notice that the shape of the cylinders share similarities to mushrooms.

In Figure 15 it is visible that the cylinders do not have the same width at all heights. Furthermore, this effect, which was seen in the samples infiltrated with four cycles, is more severe here and may affect the etching since the diameter of the etch mask will be different at different times in the etch. This may result in cylinders in the silicon with slightly positive sidewalls.
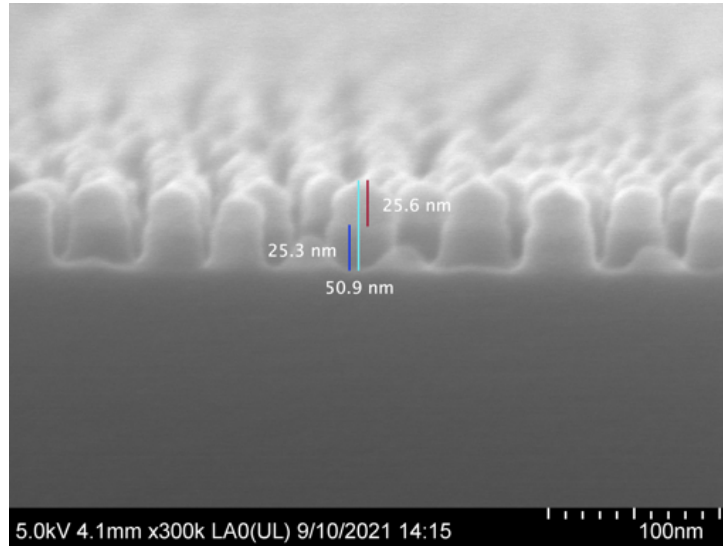
Figure 16: SEM images of the cylindrical AlO_x structures after etching of silicon. Notice the difference in contrast at approximately half the height of the pillars, indicating an interface between the etch mask and the silicon substrate.

In the figure above, notice that the sidewalls of the cylinders are not completely straight but instead has a positive slope. This might partially be due to the variable width of the etch mask at different heights in the cylinders. Of course, the obtainable anisotropy of the etching also affects the sidewall incline. From the measurements taken in Figure 15 and 16, an etch rate can be calculated for the etch mask consisting of AlO_x cylinders. This is shown below.

Etch rate in silicon: 25.3 nm in 90 s $\rightarrow$ 16.9 nm/min

Etch rate in AlO_x mask: $26.8 - 25.6 = 1.2$ nm in 90 s $\rightarrow$ 0.8 nm/min

From this data, the etch selectivity can be expressed, i.e. how much faster one material etches compared to another. For Si:AlO_x, the ratio is:

Etch selectivity (Si:AlO_x): $16.9/0.8 \approx 21 : 1$

With an etch selectivity of 21:1, it is possible to create structures with substantially larger aspect ratios than the BCP film cylinders had initially. However, because of the shape of the top of the etch mask cylinders, perhaps only around two-thirds of the etch mask might be usable as the silicon part of the cylinders will be exposed after etching that much. Furthermore, the etch selectivity might be lower at the bottom of the cylinders which may obtain less AlO_x during infiltration. Moreover, to archive a good NIL stamp, the remaining AlO_x might need to be removed. This can be achieved by either using a wet etch or by slightly over etching the sample.

Notice that the parameters used during infiltration might affect the amount of alumina infiltrated, as well as the quality in terms of density, homogeneity and shape. Hence, the obtained etch rate is only applicable with certainty to samples with the same infiltration parameters. Therefore, it is advisable to perform etch rate measurements during the etching for all the samples. Furthermore, the difference in etch rates will provide useful information as to which infiltration parameters are preferable to use.

Since all infiltrated samples have cylinders of roughly the same height as the BCP film, 27 nm, we can calculate an approximate value of the maximum etching time before the etch mask is completely removed, assuming the etch rate, 0.8 nm/min, will be roughly equal for the different samples.

$$27 \text{ nm } \cdot \text{ } 0.8^{-1} \text{ nm}^{-1} \cdot \text{min} = 33 \text{ min } 45 \text{ s}.$$

With this in mind it is possible to approximate the highest achievable aspect ratio for the cylinders. Since the etch mask will be completely removed after 33 min and 45 s, the height of the cylinders can be calculated using the silicon etch rate, 16.9 nm/min.

$$33.75 \text{ min } \cdot 16.9 \text{ nm} \cdot \text{min}^{-1} = 570 \text{ nm}.$$

Assuming the width of the cylinders remains the same, around 21 nm, this would result in an aspect ratio (height:width) of around 27:1. To obtain this number, lots of assumptions were made. For example, etching half a micron without a visible positive slope is acutely difficult. Furthermore, as mentioned before, since the etch mask takes on a triangular shape at the top, one-third of the mask might not be usable as an etch mask, significantly reducing the height and aspect ratio feasible. Therefore, the maximum practical etch dept using infiltrated AlO_x would be interesting to explore.

4.4 Manufacturing the NIL Stamp

In the last stage of the Master's thesis project, two four-inch silicon wafers were manufactured into NIL stamps by using reasonable processing conditions, found during the thesis project. 200°C was the temperature where the best etch selectivity between the mask and silicon was obtained. However, at this high temperature, thermal annealing affected the pattern created by SVA. Since the self-assembly using thermal annealing was never sufficiently optimised, resulting in poor coverage of the cylindrical pattern, this infiltration temperature is not suitable for the NIL stamp fabrication. The reason for this is that bacteria might survive on the unpatterned parts of the sample where no cylinders were present after SIS. Moreover, since there was no clear difference in the etch results between the remaining infiltration temperatures investigated, 90°C was chosen as the infiltration temperature for the NIL stamp fabrication since most knowledge of the etch rate was at this infiltration temperature. Due to the large size of the sample, ashing and etching times were increased from the optimal times found slightly to account for higher usage of the reactive ion species during etching. Both polymer ashing and etching was carried out for 3.5 minutes. After the etching, fluor deposition removal was carried out for three minutes, using the same recipe as the polymer ashing.

There was not enough time to capture micrographs of polymer films created using these samples as NIL stamps. However, an earlier sample, before SIS optimisation was completed, was brought through the whole process from BCP film to usage as a NIL stamp, to show that the process, as presented in Figure 3, was possible. Images from an imprinted polymer film where this sample was used as a NIL stamp is presented in Figure 17.

<center>(a)   (b)</center>
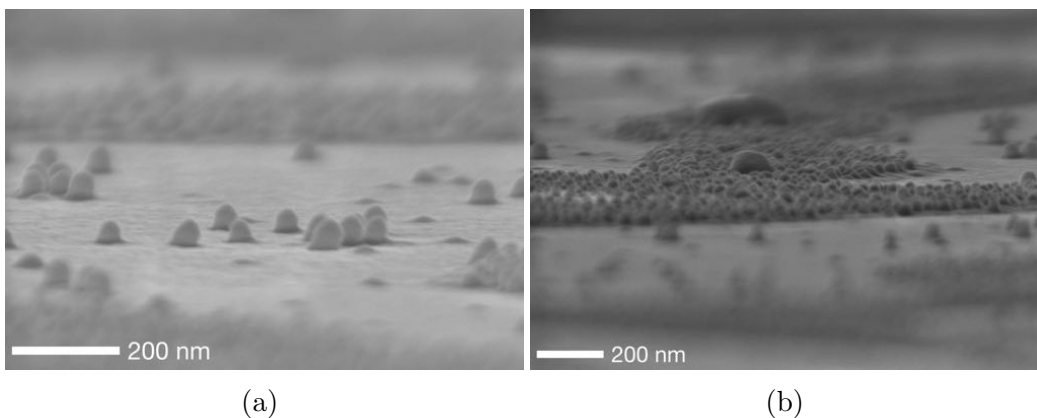
Figure 17: SEM images of the polymer film after nanoimprint lithography has been performed. Notice that the edges of the cylinders have become rounded as a result of the NIL processing as compared to the shape of etched structures shown earlier.

Looking at these images, it is evident that pattern transfer has taken place. This means the whole process, starting from a BCP film and ending with an imprinted polymer film works. It is also clear that the NIL process results in cylinders with rounded edges, as the etched structures had substantially sharper edges. Islands containing no cylinders are seen in the images above, meaning this stamp is likely not antibacterial but remember, this NIL stamp was made before optimisation of the process was completed. In the four-inch stamps manufactured, no islands were observed.

<center>42</center>

5 Conclusions and Outlook

In this Master's thesis project, optimisation of sequential infiltration synthesis has been conducted. There was no substantial difference in dimensions of the cylinders after infiltration at 90, 100 and 145°C. For the sample infiltrated at 200°C, the height of the cylinders was affected. After subsequent etching, it was found that the sample infiltrated at 200°C resulted in a greater height and aspect ratio as compared to the three other samples where no significant difference was found. During this Master's thesis project, thermal annealing was observed to induce self-assembly of the BCP PS-b-P4VP into perpendicularly aligned cylinders that were locally hexagonally placed. As mentioned in Section 2.1.3, this has not been reported in the published literature according to the Master students best knowledge, however, a combination of SVA and thermal annealing has been shown to induce self-assembly earlier.

The etch rate and selectivity were obtained for infiltration at 90°C for eight cycles. The selectivity between the etch mask and silicon (Si:AlO$_x$) was 21:1.

In this Master's thesis project, usage of a BCP film combined with sequential infiltration synthesis and etching has been shown as a possible route to manufacturing a nanoimprint lithography stamp with which transfer of the cylindrical pattern into a polymer film is possible.

This Master's thesis project could have easily been carried out for multiple more months to further study the optimal self-assembly, infiltration, and etching conditions. One of the more interesting parts to study further is the use of thermal annealing to induce the self-assembly of the BCP film directly in the ALD chamber. For example, it would be interesting to find whether sufficient coverage of the microphase separated pattern could be achieved by using a thicker BCP film. Furthermore, examination of the best annealing temperature and how long the thermal annealing should be carried out before infiltration starts are interesting and the effects it has on pattern quality and coverage. Another interesting aspect to study is if one cycle of infiltration at 90°C could be combined with subsequent cycles at 200°C to lock the SVA-induced pattern into place during the first cycle while the following cycles allow for maximum AlO$_x$ infiltration.

A Sequential Infiltration Synthesis Recipes

The recipe used for infiltration can be seen in the table below. It is general for all the infiltrations performed as the only parameter that was changed was the temperature, which is denoted with an x in the table. When this recipe was used in the ALD, the x was simply replaced with the actual temperature used for the respective sample.

Table 3: The recipe used during infiltration. Notice that the x on row 3 and 4 denotes the respective temperatures used during the infiltration optimisation.

	Instruction	#	Value	Units
0	flow		5	sccm
1	heater	6	150	°C
2	heater	7	150	°C
3	heater	8	x	°C
4	heater	9	x	°C
5	heater	10	115	°C
6	stabilise	8		
7	stabilise	9		
8	wait		1200	s
9	pulse	1	0,015	s
10	wait		0,8	s
11	goto	9	100	
12	wait		90	s
13	pulse	0	0,010	s
14	wait		0,8	s
15	goto	13	50	
16	wait		600	s
17	goto	9	4	
18	flow		5	sccm

B   Reactive Ion Etching Recipes

The recipe used for polymer ashing can be seen in Table 4. Notice that the time parameter under the etch step was changed for some of the samples.

Table 4: Recipe used for the polymer ashing.

	Initial	Chuck	Etch step	Dechuck	End
Time	0:10.0		2:30.0		0:10.0
Pressure	0.1	3.0	3.0	0.0	0.1
N_2		0	0	0	
H_2		0	0	0	
SF_6		0	0	0	
CHF_3		0	0	0	
CF_4		0	0	0	
C_4F_8		0	0	0	
Ar		0	0	0	
O_2		30	30	0	
RF		0	25	0	
ICP		0	10	0	

The recipe used for etching can be seen in the table below. It is general for all the etches performed, meaning the time parameter under the etch step was chosen after the amount etching wanted for each specific sample.

Table 5: Recipe used for etching. Notice that the etch step was changed depending on the amount of etching required.

	Initial	Chuck	Gas stab	Ignition	Etch step	Evac step	Dechuck	End
Time	0:10.0		0:10.0	0:05.0	1:00.0	0:10.0		0:10.0
Pressure	0.1	1.0	5.0	5.0	5.0	0.1	1.0	0.1
N_2		0	0	0	0		0	
H_2		0	0	0	0		0	
SF_6		0	26	26	26		0	
CHF_3		0	0	0	0		0	
CF_4		0	0	0	0		0	
C_4F_8		0	54	54	54		0	
Ar		0	20	20	20		0	
O_2		0	0	0	0		0	
RF		0	0	25	25		0	
ICP		0	0	0	300		0	

C   Nanoimprint Lithography Processing

The processing steps to create the film that was examined for antibacterial properties are presented below.

1. Starting material: Anti-stick treated silicon stamp containing pillars.

2. Spin-coat Obducat NIL-IPS-resist 'solution 8' on a PC-film.

   (a) Solution 8: 500 rpm, 5 s, 500 rpm/s + 3000 rpm, 30 s, 1000 rpm/s, no soft bake.

3. UV-imprint the PC+solution 8-IPS with the Si-stamp.

   (a) If the stamp is smaller than the IPS, protect the NIL chuck with a piece of the thermal IPS material.

   (b) Imprint with the IPS on top of the stamp, deposit the IPS on the stamp by using a roller.

   (c) UV-NIL parameters: room temperature, 20 bar, 60 s flow + 180 s exposure.

4. PECVD-antisticking of the PC+solution 8-IPS in Obducat's PECVD-antisticking equipment.

   (a) Anti-sticking thickness control by including a silicon test piece that is measured with an ellipsometer.

   (b) Parameters: $p_0 \approx$ 1-3$\cdot 10^{-5}$ mbar, flow $= 30$ sccm of fluoro-carbon anti-sticking molecule gas, $p = 100$ mTorr, 60 s stabilisation time, $P = 30$ W, $t = 120$ s.

5. Cut a suitably sized PET-film to be used as a substrate, consider the available sizes of the chucks for spin-coating.

   (a) A substrate size of at least a few mm larger than the spin-chuck is typically a good choice to minimise sticky resist on the backside of the substrate.

6. UV-ozone treatment on the PET-substrate for improved resist adhesion.

   (a) 70°C, 5 min.

   (b) Perform this step just before the spin-coating in the next step.

7. Spin-coating Obducat NIL-STU-resist 'TU7' on the PET-substrate, soft bake on a hotplate.

   (a) The residual layer thickness is not critical here. A thickness of a few hundred nm can be suitable which can cover small defects on the PET-film with resist.

   (b) 500 rpm, 5 s, 500 rpm/s + 3000 rpm, 30 s, 1000 rpm/s + 95°C, 2 min on hotplate.

8. STU-imprint with the PECVD-antisticked PC+solution 8-IPS in TU7 on the PET-substrate.

   (a) Result: Pillars in TU7 on the substrate.

   (b) Use a large blank Si-wafer as a backplate and place the PET-substrate with TU7 and the IPS on top. Use the roller when depositing the IPS on the substrate.

(c) STU: 65°C, 20 bar, 60 s flow + 180 s exposure, -1, -1: (the Obducat Eitre 6 nanolab process).

9. Inspection of the imprint results.

   (a) Look for significant defects, like larger particles, air inclusions and TU7-film rip-off from the PET carrier substrate.

   (b) Visual check with an inspection lamp and an optical microscope.

   (c) Optional: AFM and/or SEM (for SEM, first sputter a thin layer of PtPd or Ir).

   (d) For detailed pattern inspection, it can be better to also process a Si-wafer with TU7 in the same way in parallel with the PET-substrate. This can then be used for characterisation, in particular for SEM cross-section inspection.

References

[1] Kim JK, Yang SY, Lee Y, Kim Y. Functional nanomaterials based on block copolymer self-assembly. Progress in Polymer Science. 2010;35(11):1325–1349.

[2] Rahikkala A, Soininen AJ, Ruokolainen J, Mezzenga R, Raula J, Kauppinen EI. Self-assembly of PS-b-P4VP block copolymers of varying architectures in aerosol nanospheres. Soft Matter. 2013;9(5):1492–1499.

[3] Morris M. Directed self-assembly of block copolymers for nanocircuitry fabrication. Microelectronic Engineering. 2015;132:207–217.

[4] Kim SH, Misner MJ, Russell TP. Solvent-induced ordering in thin film diblock copolymer/homopolymer mixtures. Advanced Materials. 2004;16(23-24):2119–2123.

[5] Guarini KW, Black CT, Yeung SH. Optimization of diblock copolymer thin film self assembly. Advanced Materials. 2002;14(18):1290–1294.

[6] Chaudhari A, Ghoshal T, Shaw MT, Cummins C, Borah D, Holmes JD, et al. Formation of sub-7 nm feature size PS-b-P4VP block copolymer structures by solvent vapour process. In: Advances in Patterning Materials and Processes XXXI. vol. 9051. International Society for Optics and Photonics; 2014. p. 905110.

[7] Matsen MW, Schick M. Stable and unstable phases of a diblock copolymer melt. Physical Review Letters. 1994;72(16):2660.

[8] Klok HA, Lecommandoux S. Supramolecular materials via block copolymer self-assembly. Advanced Materials. 2001;13(16):1217–1229.

[9] Tseng YC, Darling SB. Block copolymer nanostructures for technology. Polymers. 2010;2(4):470–489.

[10] Simao C, Francone A, Borah D, Lorret O, Salaun M, Kosmala B, et al. Soft graphoepitaxy of hexagonal PS-b-PDMS on nanopatterned POSS surfaces fabricated by nanoimprint lithography. Journal of Photopolymer Science and Technology. 2012;25(2):239–244.

[11] Posselt D, Zhang J, Smilgies DM, Berezkin AV, Potemkin II, Papadakis CM. Restructuring in block copolymer thin films: In situ GISAXS investigations during solvent vapor annealing. Progress in polymer science. 2017;66:80–115.

[12] Kamcev J, Germack DS, Nykypanchuk D, Grubbs RB, Nam CY, Black CT. Chemically enhancing block copolymers for block-selective synthesis of self-assembled metal oxide nanostructures. ACS nano. 2013;7(1):339–346.

[13] Yu X, Han Y. Thermal and solvent annealing of block copolymer films. In: Directed Self-assembly of Block Co-polymers for Nano-manufacturing. Elsevier; 2015. p. 47–66.

[14] Cui Z. Nanofabrication: Principles, Capabilities and Limits. Springer US; 2009. Available from: https://books.google.se/books?id=cCGU7Lwn-noC.

[15] Park S, Lee DH, Xu J, Kim B, Hong SW, Jeong U, et al. Macroscopic 10-terabit–per–square-inch arrays from block copolymers with lateral order. Science. 2009;323(5917):1030–1033.

[16] Nieswandt K, Georgopanos P, Abetz V. Well-defined polyvinylpyridine-block-polystyrene diblock copolymers via RAFT aqueous-alcoholic dispersion polymerization: Synthesis and isoporous thin film morphology. Polymer Chemistry. 2021;12(15):2210–2221.

[17] Elmaci A, Hacaloglu J. Thermal degradation of poly (vinylpyridine) s. Polymer degradation and stability. 2009;94(4):738–743.

[18] Faravelli T, Pinciroli M, Pisano F, Bozzano G, Dente M, Ranzi E. Thermal degradation of polystyrene. Journal of analytical and applied pyrolysis. 2001;60(1):103–121.

[19] Wang HS, Kim KH, Bang J. Thermal Approaches to Perpendicular Block Copolymer Microdomains in Thin Films: A Review and Appraisal. Macromolecular rapid communications. 2019;40(4):1800728.

[20] Yang GW, Wu GP, Chen X, Xiong S, Arges CG, Ji S, et al. Directed self-assembly of polystyrene-b-poly (propylene carbonate) on chemical

patterns via thermal annealing for next generation lithography. Nano letters. 2017;17(2):1233–1239.

[21] Lin Y, Böker A, He J, Sill K, Xiang H, Abetz C, et al. Self-directed self-assembly of nanoparticle/copolymer mixtures. Nature. 2005;434(7029):55–59.

[22] Leng CZ, Losego MD. Vapor phase infiltration (VPI) for transforming polymers into organic–inorganic hybrid materials: a critical review of current progress and future challenges. Materials Horizons. 2017;4(5):747–771.

[23] Weisbord I, Shomrat N, Azoulay R, Kaushansky A, Segal-Peretz T. Understanding and Controlling Polymer–Organometallic Precursor Interactions in Sequential Infiltration Synthesis. Chemistry of Materials. 2020;32(11):4499–4508.

[24] Cara E, Murataj I, Milano G, De Leo N, Boarino L, Ferrarese Lupi F. Recent Advances in Sequential Infiltration Synthesis (SIS) of Block Copolymers (BCPs). Nanomaterials. 2021;11(4):994.

[25] Peng Q, Tseng YC, Darling SB, Elam JW. A route to nanoscopic materials via sequential infiltration synthesis on block copolymer templates. Acs Nano. 2011;5(6):4600–4606.

[26] Lee SM, Pippel E, Moutanabbir O, Gunkel I, Thurn-Albrecht T, Knez M. Improved mechanical stability of dried collagen membrane after metal infiltration. ACS applied materials & interfaces. 2010;2(8):2436–2441.

[27] Gong B, Peng Q, Jur JS, Devine CK, Lee K, Parsons GN. Sequential vapor infiltration of metal oxides into sacrificial polyester fibers: shape replication and controlled porosity of microporous/mesoporous oxide monoliths. Chemistry of Materials. 2011;23(15):3476–3485.

[28] Azoulay R, Shomrat N, Weisbord I, Atiya G, Segal-Peretz T. Metal oxide heterostructure array via spatially controlled–growth within block copolymer templates. Small. 2019;15(51):1904657.

[29] Lim H, Suh BL, Kim MJ, Yun H, Kim J, Kim BJ, et al. High-performance, recyclable ultrafiltration membranes from P4VP-assisted

dispersion of flame-resistive boron nitride nanotubes. Journal of membrane science. 2018;551:172–179.

[30] Cummins C, Ghoshal T, Holmes JD, Morris MA. Strategies for inorganic incorporation using neat block copolymer thin films for etch mask function and nanotechnological application. Advanced Materials. 2016;28(27):5586–5618.

[31] Wang X, Chen Y, Wang L, Cui Z. Fabrication of nanoimprint template in Si with high etch rate by non-switch DRIE process. Microelectronic engineering. 2008;85(5-6):1015–1017.

[32] Mirza MM, Zhou H, Velha P, Li X, Docherty KE, Samarelli A, et al. Nanofabrication of high aspect ratio (50: 1) sub-10 nm silicon nanowires using inductively coupled plasma etching. Journal of Vacuum Science & Technology B, Nanotechnology and Microelectronics: Materials, Processing, Measurement, and Phenomena. 2012;30(6):06FF02.

[33] Schift H. Nanoimprint lithography: An old story in modern times? A review. Journal of Vacuum Science & Technology B: Microelectronics and Nanometer Structures Processing, Measurement, and Phenomena. 2008;26(2):458–480.

[34] Chou SY, Krauss PR, Renstrom PJ. Imprint of sub-25 nm vias and trenches in polymers. Applied physics letters. 1995;67(21):3114–3116.

[35] Haisma J, Verheijen M, Van Den Heuvel K, Van Den Berg J. Mold-assisted nanolithography: A process for reliable pattern replication. Journal of Vacuum Science & Technology B: Microelectronics and Nanometer Structures Processing, Measurement, and Phenomena. 1996;14(6):4124–4128.

[36] Maximov I, Sarwe EL, Beck M, Deppert K, Graczyk M, Magnusson M, et al. Fabrication of Si-based nanoimprint stamps with sub-20 nm features. Microelectronic Engineering. 2002;61:449–454.

[37] Mårtensson T, Carlberg P, Borgström M, Montelius L, Seifert W, Samuelson L. Nanowire arrays defined by nanoimprint lithography. Nano letters. 2004;4(4):699–702.

[38] Ivanova EP, Hasan J, Webb HK, Truong VK, Watson GS, Watson JA, et al. Natural bactericidal surfaces: mechanical rupture of Pseudomonas aeruginosa cells by cicada wings. Small. 2012;8(16):2489–2494.

[39] Linklater DP, Baulin VA, Juodkazis S, Crawford RJ, Stoodley P, Ivanova EP. Mechano-bactericidal actions of nanostructured surfaces. Nature Reviews Microbiology. 2021;19(1):8–22.

[40] Modaresifar K, Azizian S, Ganjian M, Fratila-Apachitei LE, Zadpoor AA. Bactericidal effects of nanopatterns: a systematic review. Acta biomaterialia. 2019;83:29–36.

[41] Poly(styrene)-b-poly(4-vinylpyridine) [Webpage]. 124 Avro avenue, Dorval, Canada: Polymer Source Inc.; [cited 2022 Jan 17]. Available from: https://www.polymersource.ca/index.php?route=product/category&path=2_2190_16_105_2209_619&subtract=1&categorystart=A-2.1.9.6.3&serachproduct=.

[42] RC2 Ellipsometer [Webpage]. 311 South 7th Street, Lincoln, United States: J.A. Wollam; [cited 2022 Jan 17]. Available from: https://www.jawoollam.com/products/rc2-ellipsometer.

[43] Löfstrand A, Svensson J, Wernersson LE, Maximov I. Feature size control using surface reconstruction temperature in block copolymer lithography for InAs nanowire growth. Nanotechnology. 2020;31(32):325303.